Supplementary Material for

Measuring Hall viscosity of graphene's electron fluid

A. I. Berdyugin, S. G. Xu, F. M. D. Pellegrino, R. Krishna Kumar, A. Principi, I. Torre,
M. Ben Shalom, T. Taniguchi, K. Watanabe, I. V. Grigorieva, M. Polini,
A. K. Geim*, D. A. Bandurin*

*Corresponding author. Email: geim@manchester.ac.uk (A.K.G.); bandurin.d@gmail.com (D.A.B.)

This PDF file includes:

Supplementary Text
Figs. S1 to S6
References

#1 Device fabrication and characterization

Our devices were made of encapsulated monolayer and bilayer graphene crystals. In the fabrication process, we employed the same procedures as reported previously (*32-34*). In brief, graphene was first encapsulated between relatively thick (~50 nm) hBN crystals using the standard dry-peel technique (*33*). The resulting stack was then deposited on top of an oxidized Si wafer (290 nm of SiO_2), which served as a back gate electrode. After this, the van der Waals assembly was patterned using electron beam lithography to define contact regions. Reactive ion etching was implemented to selectively remove the areas unprotected by a lithographic mask, which resulted in trenches for depositing metal contacts to graphene. They were made by evaporating 3 nm of Cr and 80 nm of Au. The studied devices were usually endowed with a top gate. To this end, another round of electron-beam lithography was used to prepare a thin metal mask which defined a multiterminal Hall bar and, at the same time, served as a top gate electrode. Subsequent plasma etching translated the shape of this mask into graphene. For Hall bar devices without a top gate, their shape was defined in the same manner but a PMMA mask was used instead of a metal one. The devices were $2 - 4$ μm in width W and up to 20 μm in length and had several closely spaced voltage probes allowing us to study the local response at various distances L from the current injector. Optical micrographs of some of our devices are shown in Fig. 1E of the main text and figs. S1, A-B.

After fabrication, the devices were characterized using the standard four-terminal geometry. This involved measurements of their conductivity σ as a function of carrier density n and temperature T. Figs. S1, C and D show a typical field-effect behavior for our MLG and BLG devices, respectively. The charge carrier mobility μ was calculated using the Drude formula, $\mu = \sigma/ne$, and for typical $n = 10^{12}$cm^{-2} exceeded 150,000 cm^2/Vs at 4 K and remained around 100,000 cm^2/Vs at room temperature for most of our MLG and BLG devices. These values translate into the mean free path $l_{\mathrm{mfp}} = \mu\hbar/e(\pi n)^{1/2}$ of about $0.5 - 2$ μm (insets of figs. S1, C-D).

#2 Choice of the temperature range and reproducibility of the observed viscous effects

For consistency with the earlier work, we have checked that all our devices exhibited the key signatures associated with electron hydrodynamics in zero B. Those are the negative sign of the resistance measured in the vicinity geometry (inset of fig. S2A) and its nonmonotonic T dependence (*6, 7*). In agreement with the previous experiments (*6*), R_{v} first decreases with increasing T, changes its sign to become negative above $T \approx 50 - 100$ K, goes through a minimum at about $100 - 200$ K and then starts to grow, becoming positive again (fig. S2A). This behavior was universal, observed for all our high-quality devices (nearly two dozens). The origin of the nonmonotonic T dependence is well understood (*6, 7, 10, 12, 18, 35*) but let us reiterate. At low T, ballistic (single-particle) effects dominate, and the positive R_{v} signal stems from electrons reflected from the boundary opposite to the current injector and collected by

the voltage probes (7, 36). With increasing T, electron-electron scattering starts affecting the ballistic transport so that some injected electrons scatter at ambient charge carriers, preventing their thermal equilibrium with voltage probes (7, 12). This results in a negative contribution to the vicinity signal (12). As T increases, the electron-electron contribution also increases and overwhelms the one coming from the sample boundaries. Accordingly, R_{v} becomes more and more negative. Eventually, electron-electron scattering becomes sufficiently strong for the hydrodynamic description to become applicable, providing a better and simpler description of electron transport. In this regime, negative R_{v} is proportional to the electron viscosity and can be understood as entrainment of the electron fluid by the injected current, which produces negative lobes in the electrical potential ϕ in a vicinity of the injector (6, 18, 19) (see Fig. 1 of the main text). A further increase in T leads to increasingly stronger electron-electron scattering but smaller viscosity, which in turn suppresses viscous effects for the given distance L to the vicinity contact (fig. S2A). This results in the nonmonotonic dependence of R_{v}. According to the theory (7), R_{v} becomes most negative if the electron-electron scattering length l_{ee} is approximately equal L.

Because our report addresses the question of how the above hydrodynamic behavior is modified by the presence of magnetic field, we focus on the regime $l_{\mathrm{ee}} < L$ which occurs in our experiments for T between ~100 and 300 K. Nonetheless, for completeness fig. S2B shows the field dependence $R_{\mathrm{v}}(B)$ for the entire T interval. At high T of 180-240 K, the behavior is dominated by the Hall viscosity as described in the main text. At 5 K where single-electron ballistic effects dominate, the behavior is qualitatively different: $R_{\mathrm{v}}(B)$ exhibits a large positive peak close to zero B. Such low T curves agree in fine detail with theory calculations for ballistic transport in our specific geometry (36), which take into account reflections of electrons from sample boundaries. For intermediate temperatures (e.g., 60 K), we are in the crossover regime where ballistic transport is strongly affected by electron-electron scattering. In the latter case ($l_{\mathrm{ee}} > L$), theory has been developed only for zero B (7, 12), and we avoid analysis of this regime in the present work.

We emphasize that the reported behavior was highly reproducible for different devices especially above 100 K, the T range of our interest. The reason is that temperature induces universal, thermally-excited scattering so that all 'mesoscopic' (device-dependent) features that are often found at low T practically disappear. The reproducibility has been illustrated in Fig. 3C of the main text which shows the viscous Hall coefficient $\alpha_{\mathrm{VH}} = R_{\mathrm{A}}ne/B$ for 5 different devices (three MLG and two BLG) and using many different contacts that provide different L. In addition, fig. S2C shows the temperature dependences of α_{VH} which were measured for two different MLG devices but at the same n and L. The two dependences exhibit good agreement, again indicating the universal behavior of the viscous Hall effect.

We have also crosschecked that graphene devices with low μ do not exhibit any of the reported signatures of electron hydrodynamics as it is expected to be destroyed by momentum-non-conserving scattering. To this end, we fabricated a multiterminal Hall bar

3

device using graphene deposited directly onto an oxidized Si wafer (fig. S2D), which resulted in $\mu \approx 10{,}000$ cm^2/Vs, more than an order of magnitude reduction in electronic quality as compared to the encapsulated-graphene devices described above. The low-mobility device was etched into a Hall bar of the same shape as the device in Fig. 1E of the main text to allow accurate comparison between these devices. The temperature dependence $R_{\mathrm{v}}(T)$ for the low-μ device is shown in fig. S2E. It is a positive and monotonic function of T for all n, in stark contrast to the behavior in high-μ devices (see, e.g., fig. S2A). Furthermore, the low-quality device exhibited no discernable dependence of R_{v} on B (fig. S2F; cf. fig. S2B), and no Hall-like component R_{A} could be detected at any T (inset of fig. S2F). These observations for the reference low-μ device prove that both signatures of a viscous flow (negative vicinity resistance and its anomalous field dependence) are completely destroyed by impurity scattering, as expected.

#3 Viscous Hall effect in bilayer graphene

In the main text we focused mainly on MLG devices. To emphasize the universality of the reported behavior, fig. S3A shows another example of the $R_{\mathrm{A}}(B)$ dependence but this time measured for a BLG device. One can see that the curves in fig. S3A are rather similar to those in Fig. 2A of the main text for MLG. The plotted dependences are linear in B over the entire field interval up to 40 mT used in this work. The linearity corroborates the use of the viscous Hall coefficient α_{VH} to describe the anomalous Hall effect, as discussed in the main text. Furthermore, using the same analysis as in the main text, we have extracted the Hall viscosity of BLG's electron fluid. To this end, we used the experimental dependences $R_{\mathrm{A}}(B)$ in fig. S3A and the equation $\nu_{\mathrm{H}} = -R_{\mathrm{A}}\sigma_0\nu/\xi(L/\sqrt{\nu\tau})$ provided in the main text, which is valid for BLG, too. Again, σ_0 and τ were found from the standard resistivity measurements whereas $\nu \approx \nu_0$ was taken from measurements of the vicinity resistance in zero B (*6*). The results for $\nu_{\mathrm{H}}(B)$ at two characteristic T are shown in fig. S3B. One can see the Hall viscosity for BLG's electron fluid behaves similar to that in MLG and exhibits comparable values (cf. Fig. 3, A-B of the main text).

#4 Current and potential distribution in the Hall bar geometry

In the main text, Figs. 1A and 1B show the distribution of the electrical potential $\varphi(\mathbf{r})$ near a point contact injecting an electric current into the half-plane. Those distributions could be found analytically by solving the Navier-Stokes equation [Eq. 1 of the main text]. However, our devices had a finite width W and, to find changes in $\varphi(\mathbf{r})$ and the current density distribution $\mathbf{J}(\mathbf{r})$ for our specific experimental geometry, we have solved the Navier-Stokes equation numerically using the approach described in (*16, 18*). Examples of such calculations are given in fig. S4 that shows $\varphi(\mathbf{r})$ and $\mathbf{J}(\mathbf{r})$ in zero and finite B. At zero B (fig. S4A), a viscous

flow results in an anomalous region of negative φ in the vicinity of the current-injecting contact (red arrow). This negative lobe is accompanied by a whirlpool of the electric current (see the current lines in fig. S4), in agreement with the previous reports (*6*, *18*, *21*). A finite magnetic field (fig. S4B) causes considerable changes in $\varphi(r)$ such that the negative lobe expands and the current whirlpool becomes larger. In general, the behavior of $\varphi(r)$ with increasing B is consistent with the analytical solutions shown in Fig. 1 of the main text. Although the confinement creates current whirlpools that are absent for the half-plane geometry, it does not change qualitatively the anomalous voltage response (negative lobe) that appears near the contact to the right of the current injector in fig. S4.

#5 Anomalous negative magnetoresistance

High-mobility two-dimensional systems are known to exhibit large negative magnetoresistance (MR) at cryogenic temperatures (*26*, *27*, *37–40*). This MR is usually explained in terms of skipping orbits that appear in a magnetic field and suppress backscattering (*23*, *37*). This results in a rapid increase in conductance (decrease in resistance) above a certain magnetic field B in which the cyclotron diameter becomes comparable to the device width W. Unsurprisingly, our devices also exhibit a large negative MR at liquid-helium T and in this range of B, and it can be described in the conventional terms of skipping orbits. However, we also observed a similarly large MR at T above 200 K, which is surprising because, under these conditions, l_{mfp} becomes notably smaller than W (see inset of fig. S1), and the description in terms of ballistic transport and skipping orbits becomes objectionable. This had invited alternative explanations for a number of observations reported in literature, including negative MR at elevated T in other systems such as a two-dimensional electron gas in GaAlAs heterostructures (*26*, *27*, *37–40*). One such explanation put forward recently was in terms of electron hydrodynamics (*15*, *24*).

Following arguments similar to those in (*15*, *24*), we show below that the negative MR observed in our devices above 200 K (fig. S5) is not only consistent but also agrees quantitatively with the same hydrodynamics description that has been used to explain more direct consequences of the hydrodynamics behavior such as negative R_{v} and the viscous Hall effect. To this end, we solve the Navier-Stokes equation for a graphene strip and obtain the analytical expression (*18*)

$$\rho = \frac{\sigma_0^{-1}}{1 - 2(D_\nu/W)\tanh[W/2D_\nu]}. \tag{S1}$$

Here we have used the same no-slip boundary conditions as in the main text. This choice of boundary conditions is not essential to explain the observed behavior of R_{v} (*6*) but, as shown in (*8*), they provide somewhat better agreement between the experiment and theory for the case of a fluid flow through point contacts. Eq. S1 yields that the resistivity ρ should decrease with decreasing ν and $D_\nu = \sqrt{\nu\tau}$. Physically, this is a result of the decreasing friction between

the electron fluid and sample boundaries. It is important to note that, unlike the other observables mentioned above, negative MR in the hydrodynamic regime cannot be explained using no-stress boundary conditions. Next, we use the semiclassical expression (*16*, *24*, *25*)

$$\nu(B) = \nu_0 \frac{B_0^2}{B^2 + B_0^2} \qquad \text{(S2).}$$

The decrease of ν with increasing B, given by Eq. S2, can be qualitatively understood as follows (*25*). The kinematic viscosity is a measure of momentum transfer between fluid elements and, therefore, is proportional to the electron-electron mean free path l_{ee}. Magnetic field shortens l_{ee}, limiting it to the cyclotron diameter. The latter is inversely proportional to B and, hence, ν should drop with increasing B. Combining Eqs. S1 and S2, it is straightforward to understand why magnetic field suppresses ρ in the hydrodynamic regime.

Figure S5 plots the normalized magnetoresistance $\text{MR}(B) = [\rho(B) - \rho(0)]/\rho(0)$. The solid curves are our measurements for MLG and BLG devices whereas the dashed curves are the theoretical expectations for $\text{MR}(B)$ using Eq. S1, in which ν is defined through Eq. S2, and ν_0 is taken from the experiment (Fig. 3C). The plots show good agreement between the experiment and theory, especially at higher T where the hydrodynamic description is expected to hold better. Importantly, no fitting parameters are used for the theory curves, which suggests that the negative MR is indeed consistent with the hydrodynamic description.

#6 Local suppression of the ordinary Hall effect

There exists another geometry that allows measurements of ν_{H}. Because viscous effects are prominent only at distances of about D_ν from the region of the inhomogeneous current flow (scale of about 1 μm in our experiments; see Figs. 1A-D of the main text), one can also expect an anomalous behavior of the Hall effect if it is measured locally, close to the injector region. Indeed, we have found that the local Hall resistance R_{LH} measured as shown in the inset to fig. S6A is quite different from the ordinary Hall resistance, $R_{\text{H}} = B/ne$. The Hall resistance measured in both conventional and local geometries was found to be linear in B at all T but local measurements yielded a value suppressed by as much as $\sim 20\%$ with respect to the ordinary HE, if the distance between the current contact and the two voltage probes was $\sim D_\nu$ (fig. S6A). The observed linearity in B again allows us to define the Hall coefficients $\alpha_{\text{H}} = R_{\text{H}}/B(ne)^{-1}$ and $\alpha_{\text{LH}} = R_{\text{LH}}/B(ne)^{-1}$ (fig. S6B). For a metal with a single type of charge carriers, the ordinary HE is described by $\alpha_{\text{H}} \equiv 1$, and our measurements in the conventional Hall geometry show no deviations from the unity over the entire T range (fig. S6B). In stark contrast, the local Hall coefficient α_{LH} strongly depends on T and becomes notably smaller than the standard value of unity (fig. S6B).

Using the hydrodynamic analysis reported in the main text, we show that these deviations are caused by Hall viscosity. Indeed, it is straightforward to find that R_{LH} can be written as

$$R_{\mathrm{LH}} = R_{\mathrm{H}} + 2R_{\mathrm{A}}, \tag{S3}$$

where R_{A} is a function of ν_H as discussed in the main text. We emphasize that R_{H} and R_{A} have opposites signs so that R_{LH} should always be smaller than R_{H} and the difference increases with increasing ν_{H} and decreasing L. Furthermore, as follows from Eq. S3, simultaneous measurements of R_{LH} and R_{H} allow us to find ν_{H}, which is just an alternative protocol to that discussed in the main text. Results of the analysis using Eq. S3 are plotted in fig. S6C and compared with the $\nu_{\mathrm{H}}(T)$ dependence found from the vicinity measurements (Fig. 3B). One can see that the two approaches yield excellent agreement.
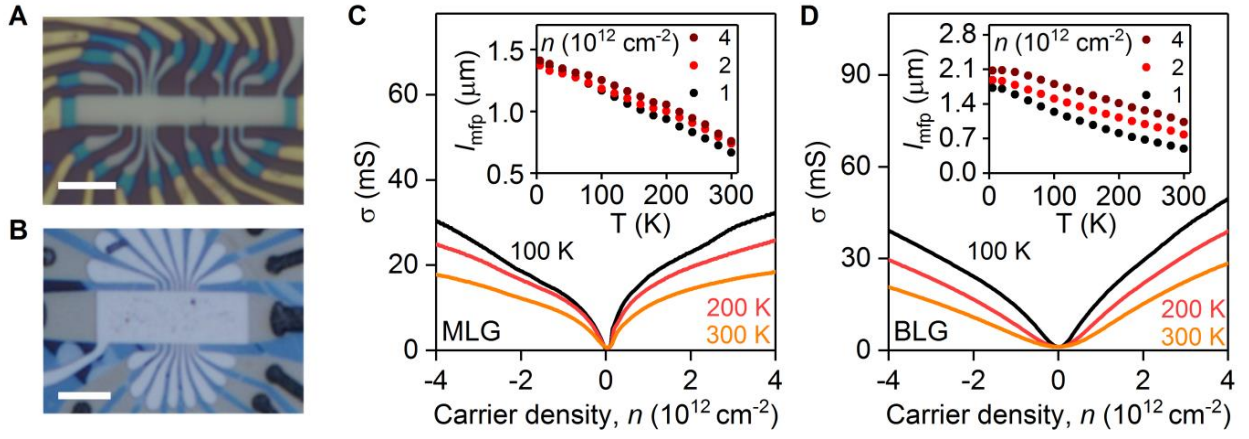
Fig. S1.

Further examples of the studied graphene devices and their behavior. (**A** and **B**) Optical micrographs of bilayer (A) and monolayer (B) devices. Graphene Hall bars repeat the shape of the top gate (white bright areas). Numerous metallic leads terminated with quasi-one-dimensional contacts to graphene are seen in a dull yellow color in (A). Other colors correspond to different etching depths of the hBN-graphene-hBN stack. Scale bars: 4 μm in both (A) and (B). (**C**) Examples of $\sigma(n)$ at a given T for the device shown in Fig. 1E of the main text. Insert: Mean free path l_{mfp} as a function of T for typical n. (**D**) Same as (C) but for BLG. The data were acquired at zero displacement field between the two graphene layers.
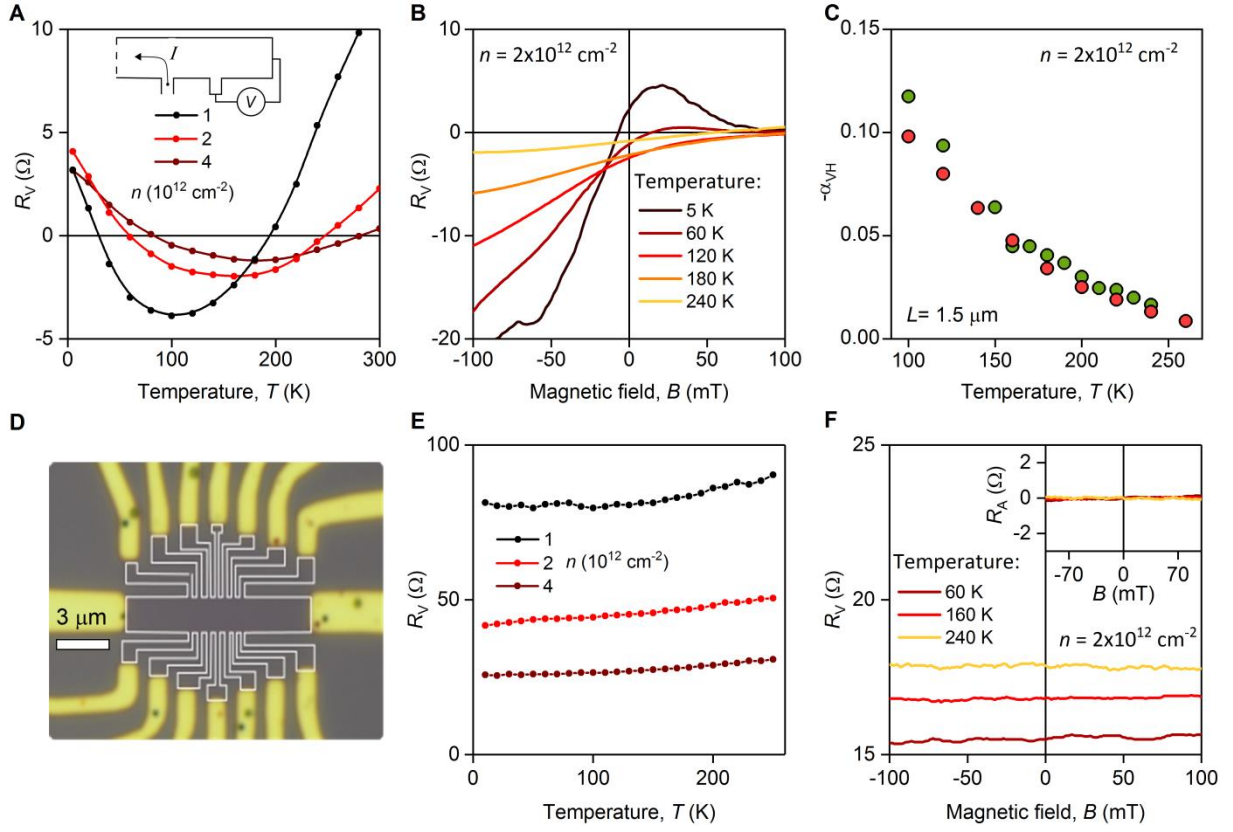
Fig. S2.

Vicinity resistance and its reproducibility. (**A**) Examples of $R_v(T)$ for the three given n away from the charge neutrality point to avoid inhomogeneous doping; $L \approx 0.7$ μm. Inset: Schematic of the vicinity geometry. (**B**) Examples of $R_v(B)$ at different T; $L \approx 1$ μm. The data in (A) and (B) are for BLG. (**C**) Viscous Hall coefficient $\alpha_{VH}(T)$ measured in two MLG devices. (**D**) Optical micrograph of a low-μ MLG device made directly on top of a Si/SiO₂ substrate. White dashed lines indicate the Hall bar mesa. (**E**) Examples of $R_v(T)$ for the device in (D); $L \approx 0.5$ μm. (**F**) $R_v(B)$ for the low-mobility device; $L \approx 1$ μm. The inset plots the antisymmetric-in-B contribution in these data.
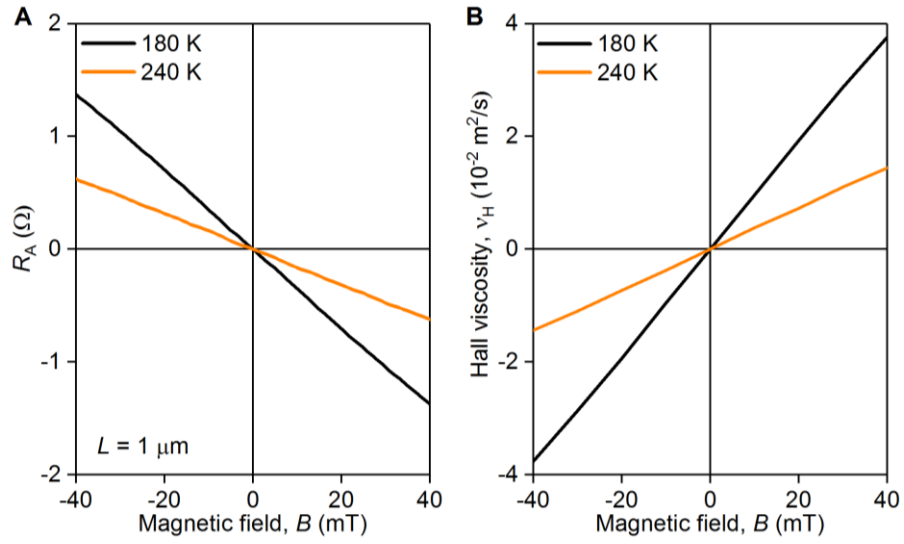
Fig. S3.

Hall viscosity of bilayer graphene. (**A**) Examples of $R_A(B)$ at the given L within the T range where the hydrodynamic description holds well. (**B**) ν_H obtained from the data in (A) using $\nu \approx \nu_0$ from Ref. (*6*) and the evaluation protocol described in the main text for MLG. $n = 2 \times 10^{12}$ cm^{-2} for both panels.
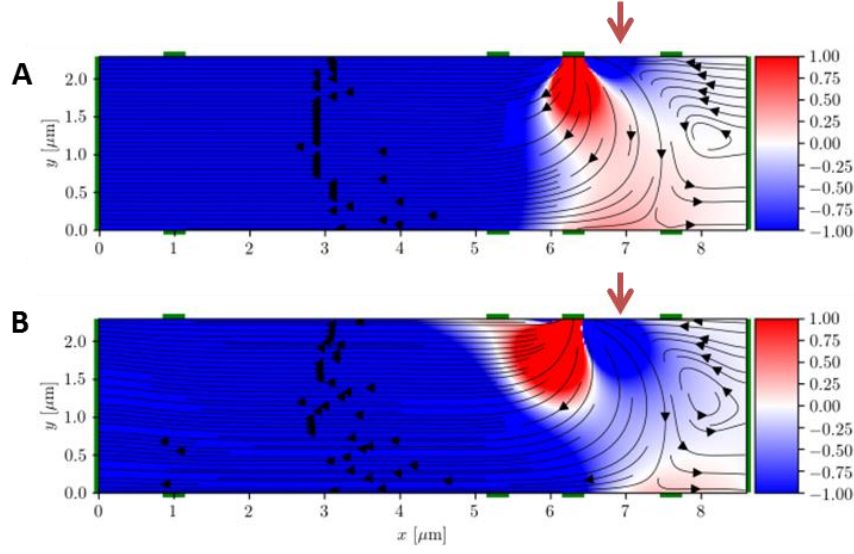
Fig. S4.

Current and voltage distributions in the Hall bars used in our experiments. (**A**) Calculated $J(r)$ and $\varphi(r)$ in the vicinity of the current injector in zero magnetic field. (**B**) Same for a finite B such as $v_{\mathrm{H}} = 2v$. The green bars indicate voltage contacts, and D_v = 1 µm for both panels. Current streamlines are shown by black curves with arrows. The thick red arrows point to the regions of the negative potential caused by the viscous flow. In (B), the trivial contribution from the ordinary Hall effect (see Fig. 1C of the main text) is subtracted to emphasize changes in the negative lobe in φ which are seen to the right from the injector in both (A) and (B). The color-coded potential is given in units of I/σ_0.
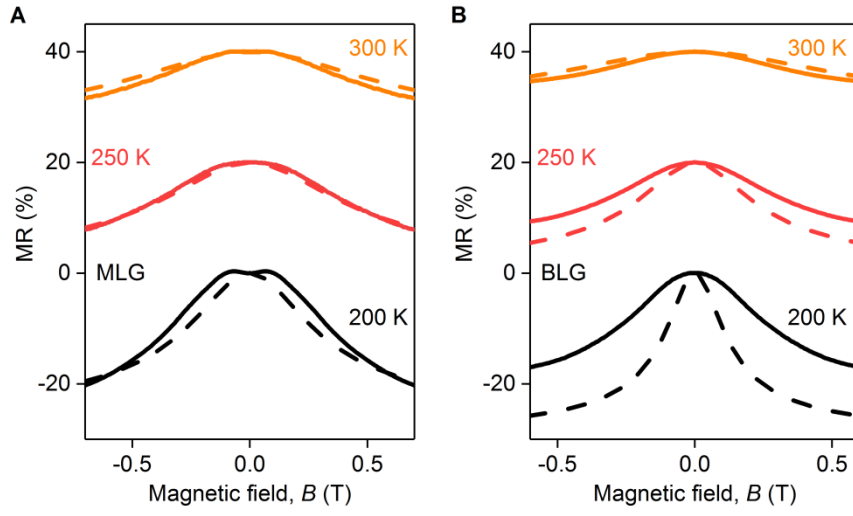
Fig. S5.

Negative magnetoresistance in the hydrodynamic regime. (**A** and **B**) MLG and BLG devices, respectively; W = 2 μm and $n = 2 \times 10^{12}$ cm^{-2}. The solid curves are experimental data. Dashed: Theory calculations using the experimental values of ν_0 and no fitting parameters. For clarity, the curves for different T are shifted by 20 %.
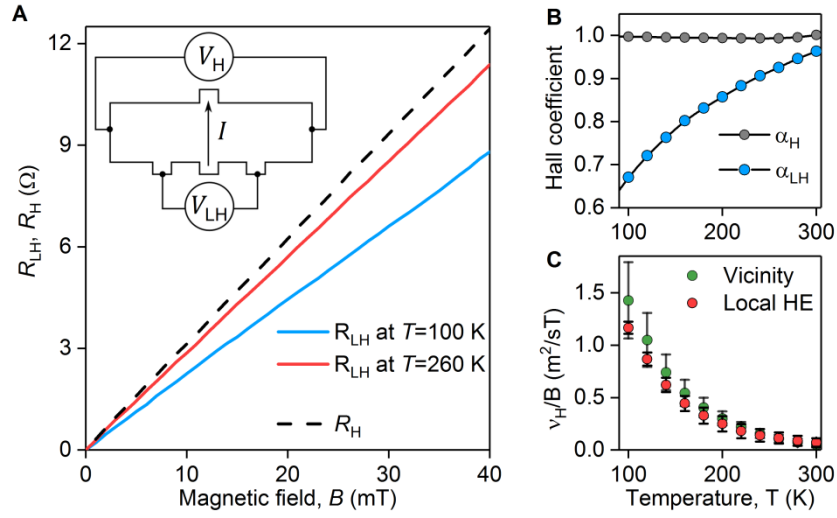
Fig. S6.

Local Hall effect. (A) Local Hall resistance R_{LH} at two T within the hydrodynamic regime (solid lines). Dashed: Conventional Hall measurements yield the classical value, $R_{\mathrm{H}} = B/ne$. Inset: Schematics of measuring R_{H} and R_{LH}. **(B)** Hall coefficients obtained from the slopes of $R_{\mathrm{H}}(B)$ and $R_{\mathrm{LH}}(B)$ such as in (A). The data are for MLG at $n = 2 \times 10^{12}$ cm^{-2} and $L \approx 1$ μm. **(C)** Comparison of v_{H}/B extracted from the local Hall and vicinity resistance measurements. The latter data are taken from Fig. 3B of the main text. Error bars: Statistics using measurements at different L for each temperature.

References and Notes

1. R. N. Gurzhi, Hydrodynamic effects in solids at low temperature. *Sov. Phys. Usp.* **11**, 255–270 (1968). doi:10.1070/PU1968v011n02ABEH003815

2. M. J. M. de Jong, L. W. Molenkamp, Hydrodynamic electron flow in high-mobility wires. *Phys. Rev. B* **51**, 13389–13402 (1995). doi:10.1103/PhysRevB.51.13389 Medline

3. A. O. Govorov, J. J. Heremans, Hydrodynamic effects in interacting Fermi electron jets. *Phys. Rev. Lett.* **92**, 026803 (2004). doi:10.1103/PhysRevLett.92.026803 Medline

4. P. J. W. Moll, P. Kushwaha, N. Nandi, B. Schmidt, A. P. Mackenzie, Evidence for hydrodynamic electron flow in $PdCoO_2$. *Science* **351**, 1061–1064 (2016). doi:10.1126/science.aac8385 Medline

5. J. Gooth, F. Menges, N. Kumar, V. Süβ, C. Shekhar, Y. Sun, U. Drechsler, R. Zierold, C. Felser, B. Gotsmann, Thermal and electrical signatures of a hydrodynamic electron fluid in tungsten diphosphide. *Nat. Commun.* **9**, 4093 (2018). [doi:10.1038/s41467-018-06688-y](doi:10.1038/s41467-018-06688-y) Medline

6. D. A. Bandurin, I. Torre, R. Krishna Kumar, M. Ben Shalom, A. Tomadin, A. Principi, G. H. Auton, E. Khestanova, K. S. Novoselov, I. V. Grigorieva, L. A. Ponomarenko, A. K. Geim, M. Polini, Negative local resistance caused by viscous electron backflow in graphene. *Science* **351**, 1055–1058 (2016). doi:10.1126/science.aad0201 Medline

7. D. A. Bandurin, A. V. Shytov, L. S. Levitov, R. K. Kumar, A. I. Berdyugin, M. Ben Shalom, I. V. Grigorieva, A. K. Geim, G. Falkovich, Fluidity onset in graphene. *Nat. Commun.* **9**, 4533 (2018). [doi:10.1038/s41467-018-07004-4](doi:10.1038/s41467-018-07004-4) Medline

8. R. Krishna Kumar, D. A. Bandurin, F. M. D. Pellegrino, Y. Cao, A. Principi, H. Guo, G. H. Auton, M. Ben Shalom, L. A. Ponomarenko, G. Falkovich, K. Watanabe, T. Taniguchi, I. V. Grigorieva, L. S. Levitov, M. Polini, A. K. Geim, Superballistic flow of viscous electron fluid through graphene constrictions. *Nat. Phys.* **13**, 1182–1185 (2017). doi:10.1038/nphys4240

9. A. Lucas, K. C. Fong, Hydrodynamics of electrons in graphene. *J. Phys. Condens. Matter* **30**, 053001 (2018). [doi:10.1088/1361-648X/aaa274](doi:10.1088/1361-648X/aaa274) Medline

10. D. Y. H. Ho, I. Yudhistira, N. Chakraborty, S. Adam, Theoretical determination of hydrodynamic window in monolayer and bilayer graphene from scattering rates. *Phys. Rev. B* **97**, 121404 (2018). doi:10.1103/PhysRevB.97.121404

11. A. Principi, G. Vignale, M. Carrega, M. Polini, Bulk and shear viscosities of the two-dimensional electron liquid in a doped graphene sheet. *Phys. Rev. B* **93**, 125410 (2016). doi:10.1103/PhysRevB.93.125410

12. A. Shytov, J. F. Kong, G. Falkovich, L. Levitov, Particle collisions and negative nonlocal response of ballistic electrons. *Phys. Rev. Lett.* **121**, 176805 (2018). doi:10.1103/PhysRevLett.121.176805 Medline

13. J. Crossno, J. K. Shi, K. Wang, X. Liu, A. Harzheim, A. Lucas, S. Sachdev, P. Kim, T. Taniguchi, K. Watanabe, T. A. Ohki, K. C. Fong, Observation of the Dirac fluid and the

breakdown of the Wiedemann-Franz law in graphene. *Science* **351**, 1058–1061 (2016). doi:10.1126/science.aad0343 Medline

14. J. E. Avron, Odd viscosity. *J. Stat. Phys.* **92**, 543–557 (1998). doi:10.1023/A:1023084404080

15. T. Scaffidi, N. Nandi, B. Schmidt, A. P. Mackenzie, J. E. Moore, Hydrodynamic electron flow and Hall viscosity. *Phys. Rev. Lett.* **118**, 226601 (2017). doi:10.1103/PhysRevLett.118.226601 Medline

16. F. M. D. Pellegrino, I. Torre, M. Polini, Nonlocal transport and the Hall viscosity of two-dimensional hydrodynamic electron liquids. *Phys. Rev. B* **96**, 195401 (2017). doi:10.1103/PhysRevB.96.195401

17. L. V. Delacrétaz, A. Gromov, Transport signatures of the Hall viscosity. *Phys. Rev. Lett.* **119**, 226602 (2017). doi:10.1103/PhysRevLett.119.226602 Medline

18. I. Torre, A. Tomadin, A. K. Geim, M. Polini, Nonlocal transport and the hydrodynamic shear viscosity in graphene. *Phys. Rev. B* **92**, 165433 (2015). doi:10.1103/PhysRevB.92.165433

19. L. Levitov, G. Falkovich, Electron viscosity, current vortices and negative nonlocal resistance in graphene. *Nat. Phys.* **12**, 672–676 (2016). doi:10.1038/nphys3667

20. G. Falkovich, L. Levitov, Linking spatial distributions of potential and current in viscous electronics. *Phys. Rev. Lett.* **119**, 066601 (2017). doi:10.1103/PhysRevLett.119.066601 Medline

21. F. M. D. Pellegrino, I. Torre, A. K. Geim, M. Polini, Electron hydrodynamics dilemma: Whirlpools or no whirlpools. *Phys. Rev. B* **94**, 155414 (2016). doi:10.1103/PhysRevB.94.155414

22. Materials and methods are available as supplementary materials.

23. C. W. J. Beenakker, H. van Houten, Quantum transport in semiconductor nanostructures. *Solid State Phys.* **44**, 1–228 (1991). doi:10.1016/S0081-1947(08)60091-0

24. P. S. Alekseev, Negative magnetoresistance in viscous flow of two-dimensional electrons. *Phys. Rev. Lett.* **117**, 166601 (2016). doi:10.1103/PhysRevLett.117.166601 Medline

25. M. S. Steinberg, Viscosity of the electron gas in metals. *Phys. Rev.* **109**, 1486–1492 (1958). doi:10.1103/PhysRev.109.1486

26. Q. Shi, P. D. Martin, Q. A. Ebner, M. A. Zudov, L. N. Pfeiffer, K. W. West, Colossal negative magnetoresistance in a two-dimensional electron gas. *Phys. Rev. B* **89**, 201301 (2014). doi:10.1103/PhysRevB.89.201301

27. V. T. Renard, O. A. Tkachenko, V. A. Tkachenko, T. Ota, N. Kumada, J.-C. Portal, Y. Hirayama, Boundary-mediated electron-electron interactions in quantum point contacts. *Phys. Rev. Lett.* **100**, 186801 (2008). doi:10.1103/PhysRevLett.100.186801 Medline

28. J. E. Avron, R. Seiler, P. G. Zograf, Viscosity of quantum Hall fluids. *Phys. Rev. Lett.* **75**, 697–700 (1995). doi:10.1103/PhysRevLett.75.697 Medline

29. I. V. Tokatly, G. Vignale, Lorentz shear modulus of a two-dimensional electron gas at high magnetic field. *Phys. Rev. B* **76**, 161305 (2007). doi:10.1103/PhysRevB.76.161305

30. F. D. M. Haldane, Geometrical description of the fractional quantum Hall effect. *Phys. Rev. Lett.* **107**, 116801 (2011). doi:10.1103/PhysRevLett.107.116801 Medline

31. A. I. Berdyugin *et al.*, Measuring Hall viscosity of graphene's electron fluid. Zenodo (2019); doi:10.5281/zenodo.2562181.

32. L. Wang, I. Meric, P. Y. Huang, Q. Gao, Y. Gao, H. Tran, T. Taniguchi, K. Watanabe, L. M. Campos, D. A. Muller, J. Guo, P. Kim, J. Hone, K. L. Shepard, C. R. Dean, One-dimensional electrical contact to a two-dimensional material. *Science* **342**, 614–617 (2013). doi:10.1126/science.1244358 Medline

33. A. V. Kretinin, Y. Cao, J. S. Tu, G. L. Yu, R. Jalil, K. S. Novoselov, S. J. Haigh, A. Gholinia, A. Mishchenko, M. Lozada, T. Georgiou, C. R. Woods, F. Withers, P. Blake, G. Eda, A. Wirsig, C. Hucho, K. Watanabe, T. Taniguchi, A. K. Geim, R. V. Gorbachev, Electronic properties of graphene encapsulated with different two-dimensional atomic crystals. *Nano Lett.* **14**, 3270–3276 (2014). [doi:10.1021/nl5006542](doi:10.1021/nl5006542) Medline

34. M. Ben Shalom, M. J. Zhu, V. I. Fal'ko, A. Mishchenko, A. V. Kretinin, K. S. Novoselov, C. R. Woods, K. Watanabe, T. Taniguchi, A. K. Geim, J. R. Prance, Quantum oscillations of the critical current and high-field superconducting proximity in ballistic graphene. *Nat. Phys.* **12**, 318–322 (2016). doi:10.1038/nphys3592

35. B. A. Braem, F. M. D. Pellegrino, A. Principi, M. Röösli, C. Gold, S. Hennel, J. V. Koski, M. Berl, W. Dietsche, W. Wegscheider, M. Polini, T. Ihn, K. Ensslin, Scanning gate microscopy in a viscous electron fluid. *Phys. Rev. B* **98**, 241304 (2018). doi:10.1103/PhysRevB.98.241304

36. M. Beconcini, S. Valentini, R. K. Kumar, G. H. Auton, A. K. Geim, L. A. Ponomarenko, M. Polini, F. Taddei, Scaling approach to tight-binding transport in realistic graphene devices: The case of transverse magnetic focusing. *Phys. Rev. B* **94**, 115441 (2016). doi:10.1103/PhysRevB.94.115441

37. S. Masubuchi, K. Iguchi, T. Yamaguchi, M. Onuki, M. Arai, K. Watanabe, T. Taniguchi, T. Machida, Boundary scattering in ballistic graphene. *Phys. Rev. Lett.* **109**, 036601 (2012). doi:10.1103/PhysRevLett.109.036601 Medline

38. A. T. Hatke, M. A. Zudov, J. L. Reno, L. N. Pfeiffer, K. W. West, Giant negative magnetoresistance in high-mobility two-dimensional electron systems. *Phys. Rev. B* **85**, 081304 (2012). doi:10.1103/PhysRevB.85.081304

39. M. Y. Melnikov, J. P. Kotthaus, V. Pellegrini, L. Sorba, G. Biasiol, V. S. Khrapai, Influence of e-e scattering on the temperature dependence of the resistance of a classical ballistic point contact in a two-dimensional electron system. *Phys. Rev. B* **86**, 075425 (2012). doi:10.1103/PhysRevB.86.075425

40. G. M. Gusev, A. D. Levin, E. V. Levinson, A. K. Bakarov, Viscous electron flow in mesoscopic two-dimensional electron gas. *AIP Adv.* **8**, 025318 (2018). [doi:10.1063/1.5020763](doi:10.1063/1.5020763)